Springer

Acta Mechanica Sinica

CrossMark click for updates

• RESEARCH PAPER •

Acta Mech. Sin., Vol. 39, 322476 (2023)
https://doi.org/10.1007/s10409-023-22476-x

Research on the primary liquid atomization mechanism of a close-coupled vortical loop slit atomizer

Min Zhang[1*], Zhaoming Zhang[2], and Qiusheng Liu[1]

[1] *Key Laboratory of Microgravity (National Microgravity Laboratory), Institute of Mechanics, Chinese Academy of Sciences, Beijing 100190, China;*

[2] *College of Aerospace Engineering, Nanjing University of Aeronautics and Astronautics, Nanjing 210016, China*

Received December 27, 2022; accepted January 19, 2023; published online April 20, 2023

To preliminarily investigate the liquid atomization (LA) process of a close-coupled vortical loop slit atomizer under realistic conditions, a numerical simulation of the flying trajectory of atomized droplets which were formed after the breaking of a metal melt and would not break anymore in the swirling flow field was carried out with the discrete phase model (DPM) based on analysis of the single-phase flow field characteristics of the gas. The results demonstrate that the radial paving scope of atomized droplets that are far away from the central axis and enter into the flow field from the source position expands at the front end of the melt delivery tube (MDT). The radial pavement scope of these atomized droplets at the front end of MDT is negatively correlated with their diameter. The recirculation zone (RZ) in the flow field of the vortical atomizer and the kinetic energy of the atomized droplets can significantly influence their flight trajectories. Moreover, two breakup models can be applied to a metal melt in a vortical atomizer—a fluctuating breakup model and a sheet breakup model.

Vortical loop slit atomizer, Swirling flow field, Discrete phase model (DPM), Atomized droplets, Breakup model

Citation: M. Zhang, Z. Zhang, and Q. Liu, Research on the primary liquid atomization mechanism of a close-coupled vortical loop slit atomizer, Acta Mech. Sin. **39**, 322476 (2023), https://doi.org/10.1007/s10409-023-22476-x

1. Introduction

Close-coupled airstream atomization is one of the primary methods used for preparing powders by breaking up liquid metals or alloys directly with an atomizing medium. An atomizer is a device that provides the atomizing medium with high energy and high speed, so it plays an important role in the efficiency and stability of the atomization process. A metal powder prepared by close-coupled airstream atomization has the characteristics of a high degree of sphericity, controllable powder grain size, and low oxygen content. Moreover, the technique is applicable to the production of a range of metal and alloy powders. Close-coupled airstream atomization has become a mainstream method with which to produce high-performance metal and special alloy powders [1]. At present, there are two major types of close-coupled atomizers. One is the two-dimensional (2D) axial symmetric loop slit (or loophole) atomizer. The other is the vortical atomizer.

Recently, the close-coupled liquid atomization (LA) mechanism has attracted extensive research attention. Key research hotspots have included the structural characteristics of an atomized flow field and the breakup (atomization) mechanism of a metal liquid flow in the recirculation zone (RZ) below the nozzle of an atomizer [2-4]. Unlike other LA techniques, close-coupled LA forms an upward-moving RZ with a very complicated flow field structure below the nozzle of the atomizer. Many researchers have discussed the interaction between the metal liquid flow and the complicated atomization flow field (breakup mechanism) in 2D axial symmetric loop slit (or loophole) atomizers. Ouyang et al. [1,5] studied the membrane formation mechanism of a metal liquid flow with an "open" wake (with an atomizing gas pressure of 2.1 MPa) due to an atomizing gas flow.

*Corresponding author. E-mail address: zhangmin@imech.ac.cn (Min Zhang)
Executive Editor: Xueming Shao

Based on a combination of traditional wave theory and fluid dynamics computing tools, Zhao [6] thoroughly investigated the primary atomization process of a metal liquid flow. Wang et al. [7] simulated the primary atomization process of airflow-atomized metal melt. Hanthanan Arachchilage et al. [8] investigated the effect of atomization gas pressure on the LA process of molten aluminum and droplet size distribution. Luo et al. [9] simulated the complex LA process to produce metal powders. Zhang et al. [10,11] conducted a numerical simulation study on the gas flow field characteristics of a vortical atomizer. However, in-depth studies of the LA mechanism of vortical atomizers are still lacking.

After the formation of atomized droplets, the kinetic energy of the atomizing gas is insufficient to offset the increasing internal energy and surface energy generated when the atomized droplets continue to break up. Therefore, the atomized droplets will not break up further [12]. The atomized droplets exchange momentum with the atomizing gas while flying. There is a strong interaction between the discrete-phase atomized droplets and the continuous-phase atomizing gas in the flight zone. The effect of the atomizing gas on atomized droplets with different diameters or speeds varies significantly, resulting in significant differences in their flight trajectories. In particular, atomized droplets with different diameters or speeds may be affected by atomizing gas in the RZ when they enter the zone. As a result, the flight trajectories of the atomized droplets change significantly.

To address the above problems, the movement of metal droplets formed after atomization that cannot break up any further is analyzed thoroughly. The aim is to provide a theoretical basis and reference with which to help understand the LA mechanism of a vortical atomizer.

2. Atomizing mechanism analysis

The flow field structure of the RZ in a 2D axial-symmetric atomizer with no metal liquid flow is shown in Fig. 1. In the RZ, the bottom-up recirculation gas changes directions at the outlet of the front end of the metal liquid flow tube and becomes a radial flow from the inside to the outside. When the recirculation gas arrives at the edges, it encounters the turbulent boundary layer and is forced to flow downward. Finally, it is restricted to within the RZ and separated from the ultrasonic velocity flow field. As a result, a RZ and a flow field out of the RZ are formed. The external flow field is separated from the RZ by a turbulence layer and a series of neighboring vortices are produced in the turbulence layer.

Gas ejected from the nozzle enters the RZ from the front end of the stagnation point (SP) and then flows out of the zone through the turbulence layer. Gas inside the RZ flows from the bottom upward, while gas coming out of the RZ

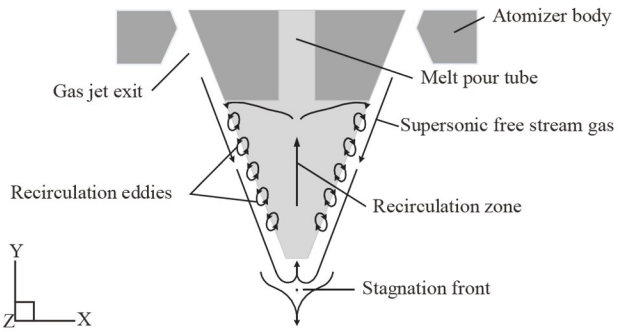

Figure 1 Flow structure of gases in the RZ of a 2D axial-symmetric atomizer [3].

flows from the top downward. Gas in the turbulence layer has a very low speed, but the mass flow of the gas is very large. Under most circumstances, the masses of the inflow and outflow gases are equal. Moreover, gas flowing in and out of the turbulence layer may not influence the pressure of the SP.

Most of the gas does not pass through the sound velocity boundaries in the RZ to enter the ultrasonic-speed atomizing gas flow. An ultrasonic-speed atomizing gas flow loses energy very easily and becomes a subsonic-speed atomizing flow, which then passes through the sound velocity boundaries and enters the subsonic-speed RZ. After some of the gas is decelerated, it is carried into the RZ from the front end of the SP. Due to the increase in the gas mass, the pressure at the outlet at the front end of the melt delivery tube (MDT) is affected. In other words, the aspiration pressure of the metal liquid flow is affected, causing pulsation.

At the front end of the SP, the gas is dragged out of vortices, accelerated to ultrasonic speeds, and passes through the sound velocity boundaries to enter the ultrasonic free-flow zone, maintaining the dynamic balance of the gas mass in the RZ. Under gas-only flow conditions, the gas flow field below the nozzle adjusts the high-speed gas flow and environmental pressure balance through expansion or compression. When the incompressible metal liquid flow is guided into the circulation zone, it breaks the original flow field balance of the compressible gases, resulting in new dynamic balance conditions for the gas flow.

In practical LA, since the RZ of the 2D axial-symmetric atomizer is close to the front end of the MDT, the primary breakup model of the metal melt is mainly determined by the local Weber number. When the Weber number is relatively small, the metal and alloy melts will keep a completely liquid core after flowing from the central hole of the front end of the MDT and will then continue to flow downward into the RZ. Subsequently, the melt interface may develop a disturbance due to a Kelvin-Helmholtz (K-H) instability under the effect of the high-speed jet stream. Such a tiny disturbance may show linear and or weakly nonlinear growth and develop into a turbulence mixture due to a

strong nonlinear effect. The internal speed of this mixture layer changes uniformly. Meiron et al. [13] analyzed this variation process carefully. In other words, large liquid droplets peel off from the liquid column surface and the whole liquid column undergoes a fluctuating breakup (see Fig. 2a). When the Weber number is relatively high, liquid metals and alloys from the central hole may flow to the gas outlet and then make direct contact with the high-speed atomized gas flow. Subsequently, the high-speed atomized gas flow may form a high-frequency small-amplitude vibration on the metal melt. Such vibration is attributed to the Rayleigh-Taylor (R-T) instability. This is also called the acting effect of short waves [14]. Mates and Settles [15,16] discovered this phenomenon experimentally (see Fig. 2b). Some scholars have shown that sheet breakup is more conducive to producing smaller atomized droplets [17].

The position of the RZ and the flow field structure in the vortical atomizer when there is no metal liquid flow are shown in Fig. 3. Due to entrainment, the surrounding gases are brought into the efflux from the gas outlet. Some of the gas flows near the front-end wall of the MDT toward the gas outlet, and some flows toward the center of the front end of the MDT. The rest flows along the negative direction of the *y*-axis. Since the high-speed gas flowing toward the center of the front end of the MDT has a centripetal pressure gradient oriented toward the *y*-axis in the radial direction, the speed of these high-speed gas flows along the *x*-axis first decreases to zero and then gradually increases in the *x*-*y* plane. When the gas flow approaches the central hole at the front end of the MDT, it flows along the negative direction of the *y*-axis. Furthermore, the gas that flows into the atomizing chamber from the central hole at the front end of the MDT flows at an accelerated speed along the negative direction of the *y*-axis as a response to the collaborative

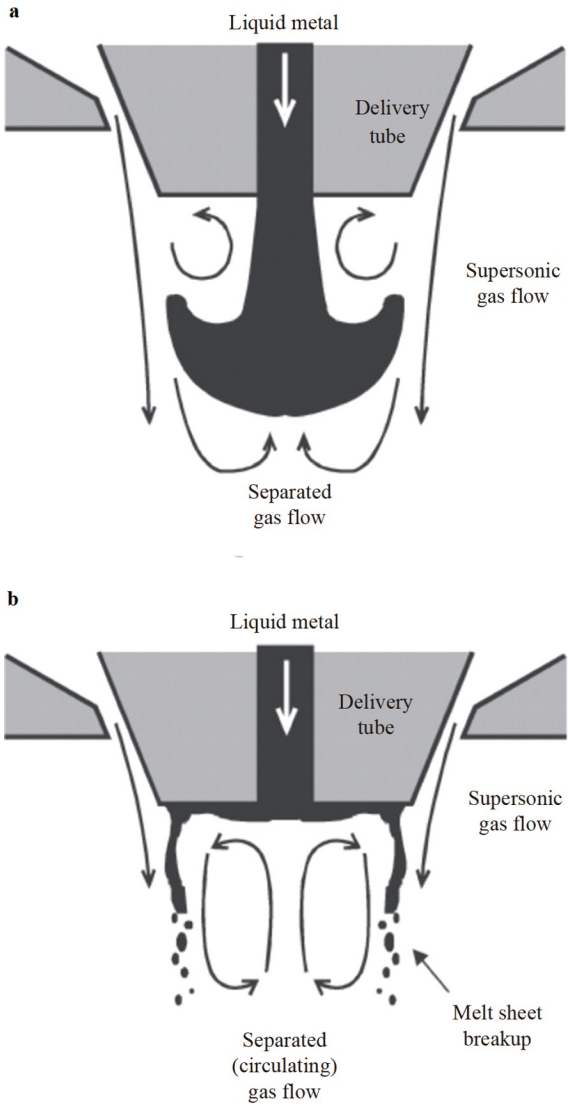

Figure 2 "fountain" and melt sheet primary breakup models [15,16]: **a** the "fountain" breakup and **b** the sheet breakup.

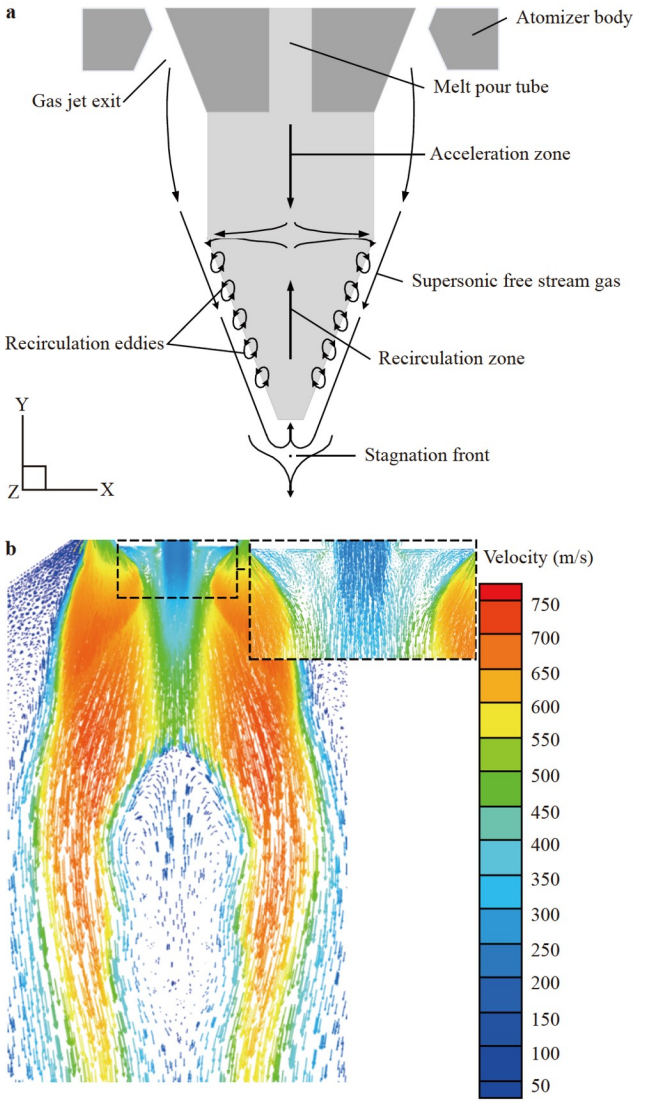

Figure 3 Flow structure and speed vector of gases in the RZ of a vortical atomizer [10,11]: **a** the flow structure and **b** the speed vector in the *x*-*y* plane.

effect of the frictional force of the surrounding high-speed gas flow in the same direction and the aspiration pressure intensity at the front end of the MDT (see Fig. 3b).

Some high-speed gas enters the RZ through the front end of the SP (where the gas flow has a speed component along the *x*-*z* direction), while the rest flows along the negative direction of the *y*-axis. The gas flow that enters the RZ may flow to the low-pressure zone at the front end of the MDT. The gas flow velocity first increases to a maximum and then gradually decreases. As the gas flow approaches the low-pressure zone, it flows along the radial direction. When gas flows at the edges of the RZ in contact with the sound speed boundaries, some of it may flow along the negative direction of the *y*-axis due to inward squeezing. This gas is then restricted to the internal side of the sound velocity boundary. The rest of the gas flow converges with the high-speed gas flow due to the effects of frictional force. Inside the RZ, the turbulence boundary layer separates the gases flowing along the negative and positive directions of the *y*-axis (see Fig. 3a).

To sum up, this study predicts using an analogical method that the metal liquid flow in the gas flow field structure of a unique vortical atomizer may develop two breakup models —a fluctuating breakup model and a sheet breakup model. The research conclusions support this prediction.

3. The movement of atomized droplets in the gas flow field

3.1 Stress analysis of the atomized droplets

Since atomized droplets have unique 3D motion features in the gas flow field of a vortical atomizer, they bear very complicated stresses. To disclose the movement of atomized droplets, a comprehensive and in-depth study on the stresses of atomized droplets is needed. As a result, the effects of several unique additional forces on atomized droplets are discussed in the following text.

(1) Centrifugal force

In the swirling flow field of an atomizer, the centrifugal force (F_c) which is produced by atomized droplets along the tangential acceleration makes the atomized droplets move outward (far away from the central axis) along the radial direction. F_c can be expressed as follows:

$$F_c = m_p \frac{V_{p\theta}^2}{r} = \frac{\pi}{6} d_p^3 \rho_p \frac{V_{p\theta}^2}{r}, \tag{1}$$

where m_p is the mass of atomized droplets, d_p is the diameter of atomized droplets, ρ_p is the density of atomized droplets, $V_{p\theta}$ is the tangential speed of atomized droplets, and r is the radial distance of atomized droplets to the central axis. Based on dimensional analysis, the centrifugal force is thousands times of gravity [18], so the effects of gravity of atomized droplets on their flying trajectory in the swirling flow field during practical LA can be ignored. Hence, the gravity of atomized droplets is not considered in this study.

(2) Apparent mass force

The apparent mass force (F_x), also known as the additional mass force, is caused by facilitating the acceleration of fluids around the droplets. It can be expressed as [19]

$$F_x = \frac{1}{2} \frac{\rho_f}{\rho_p} \frac{\mathrm{d}}{\mathrm{d}t} \left(V_f - V_p \right), \tag{2}$$

where the additional mass force can be ignored when $\rho_f > \rho_p$. Since the continuous-phase fluids in this study are nitrogen, and the discrete-phase metal droplets are liquid metal aluminum (Al). In this case, $\rho_p > \rho_f$. Therefore, it does not need to consider the effect of such additional mass force. If F_x is caused by the pressure gradient in the flow field, its expression [20] is

$$F_x = \left(\frac{\rho_f}{\rho_p} \right) V_p \frac{\partial V_f}{\partial x}. \tag{3}$$

Since there is a strong pressure gradient in the flow field in this study, the effect of such an additional mass force has to be taken into account.

(3) Magnus force

In the swirling flow field, the speeds of atomizing gas surrounding the atomized droplets are different, atomized droplets may rotate as a response to the boundary layer. This drives the acceleration of surrounding atomizing gas at the side with high relative speed, while the other side shows the opposite. According to the law of conservation of energy, the pressure intensity of the atomizing gas at the side with accelerated atomizing gas surrounding the atomized droplets decreases, while the pressure intensity on the other side increases. Such pressure intensity difference will produce an acting force that will promote the movement of atomized droplets toward the acceleration side of atomizing gas. At the same time, atomized droplets rotate around themselves. This is called the Magnus effect and the produced force is the Magnus force. The expression of the Magnus force [21] is

$$F_M = k \rho_f d_p^3 \omega u_{pf}, \tag{4}$$

where F_M is the Magnus force and k is a dimensionless constant coefficient. The latter can take a value of 0.09 for large atomized droplets or $\pi/8$ for small atomized droplets [21]. As a result, the effect of the Magnus force is more significant for small atomized droplets. ρ_f is the density of the atomizing gas, ω is the angular velocity of rotation of the atomized droplets, and u_{pf} is the velocity of the atomized droplets relative to the atomizing gas, which is often called the sliding velocity.

(4) Thermophoretic force

The thermophoretic force, or called as thermotropic migration force or radiation force, is mainly produced when suspending droplets in the gas flow field with temperature

gradients undertake an opposite acting force from the gas temperature gradient. The thermophoretic force [22] is expressed as

$$F_T = -D_{T,p}\frac{1}{m_p T}\frac{\partial T}{\partial x}, \tag{5}$$

where $D_{T,p}$ is the thermophoretic force coefficient and T is the local gas temperature in the continuous-phase flow field. $D_{T,p}$ can be replaced by a constant, a polynomial, or a user-defined function (UDF). Because there is a strong temperature gradient in the flow field, the effect of the thermophoretic force has to be considered.

In a word, the flying trajectory of discrete-phase atomized droplets in the flow field is sensitive to the resistance of the continuous-phase atomizing gas (F_d), the centrifugal force (F_c), the radial pressure gradient force (F_p), the Saffman lift force (F_L) [23], the radial Basset force (F_B) [24], the Magnus force (F_M), and the thermophoretic force (F_T) (see Fig. 4). According to the estimation of the order of magnitude, atomized droplets are mainly influenced by the resistance of the atomizing gas, the centrifugal force, the radial pressure gradient force, the Magnus force, and the thermophoretic force. Hence, the following text focuses on the influence of these five forces on the flying trajectories of atomized droplets in the swirling flow field.

$$F_L = \frac{K\mu}{4}\left|V_f - V_p\right| d_p^2 \sqrt{\frac{1}{\nu}\left|\frac{\partial(V_f - V_p)}{\partial r}\right|}, \tag{6}$$

where K = 6.46 (a dimensionless constant based on numerical integration), μ is the dynamic viscosity coefficient of the gas, ν is the kinematic viscosity coefficient of the gas, and V_f and V_p are the local gas and particle velocity vectors [23].

$$F_B = 6d_p^2\rho_f\sqrt{\pi\nu}\int_{t_{p_0}}^{t_p} K_B\left(t_p-\tau\right)\left|\frac{\mathrm{d}\left(V_f - V_p\right)}{\mathrm{d}\tau}\right|\mathrm{d}\tau, \tag{7}$$

where t_p is the time coordinate, τ is a dummy integration variable, and $K_B(t_p - \tau)$ is called the Basset kernel and it is usually represented by the standard expression $1/\sqrt{t_p-\tau}$ [24].

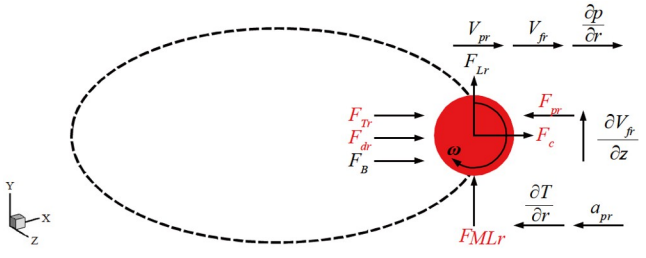

Figure 4 Stresses on the flying atomized droplets in the swirling flow field.

3.2 Gas-liquid system analysis

The deformation and breakup processes of atomized droplets during practical LA are vital to the whole atomization system. However, this study only focused on only atomized droplets that stop deformation and breakup, with considerations to deformation and mass changes of the atomized droplets. In the early stage of the movement, the speed of atomized droplets is relatively lower than that of the high-speed ejected atomizing gas and it can be ignored. Moreover, interaction forces among atomized droplets are ignored. Based on the above hypotheses, Pilch et al. [25] have proposed the relationship between the displacement of atomized droplets in the flow field and the drag force:

$$\frac{s}{d_p} = \frac{3}{8}C_d T_N^2 + BT_N^3, \tag{8}$$

$$\frac{V_p}{u_{fp}\xi^{0.5}} = \frac{3}{4}C_d T_N + 3BT_N^2, \tag{9}$$

$$\frac{ad_p}{u_{fp}^2\xi} = \frac{3}{4}C_d + 6BT_N, \tag{10}$$

where s is the displacement of atomized droplets, C_d is the mean drag force coefficient, B is the empirical parameter, u_{fp} is the initial speed of atomizing gas in relation to atomized droplets, and a denotes the accelerated velocity of atomized droplets. T_N is a dimensionless time characteristic, and it is given according to the R-T or K-H instability:

$$T_N = t_N\frac{u_{fp}\xi^{0.5}}{d_p}, \tag{11}$$

where t_N is the dimensionless time, while ξ is the mass density ratio between the atomizing gas and the atomized droplets:

$$\xi = \frac{\rho_f}{\rho_p}. \tag{12}$$

Here, the drag force is equivalent to the drag force of a steel ball with the same volume and constant mass. Numerical values of C_d as well as B [25] are

$$C_d = 1,\ B = 0.116 \text{ (compressible fluid)}, \tag{13}$$

$$C_d = 0.5,\ B = 0.0758 \text{ (incompressible fluid)}. \tag{14}$$

When analyzing the flying trajectories of atomized droplets based on the discrete phase model (DPM), the diameter of atomized droplets ranged between 3-200 μm [6,26] in this study. Nevertheless, the single-phase atomizing gas flow field has to be calculated before using the DPM. As a result, the single-phase atomizing gas flow field was calculated by using an atomizer with the protrusion length of the MDT H = 1 mm and the annular slit width D = 1.2 mm under the atomizing gas pressure intensity of P = 5 MPa (the detailed numerical simulation method is introduced in Ref. [10]). Results are shown in Fig. 5. Clearly, there is a sound

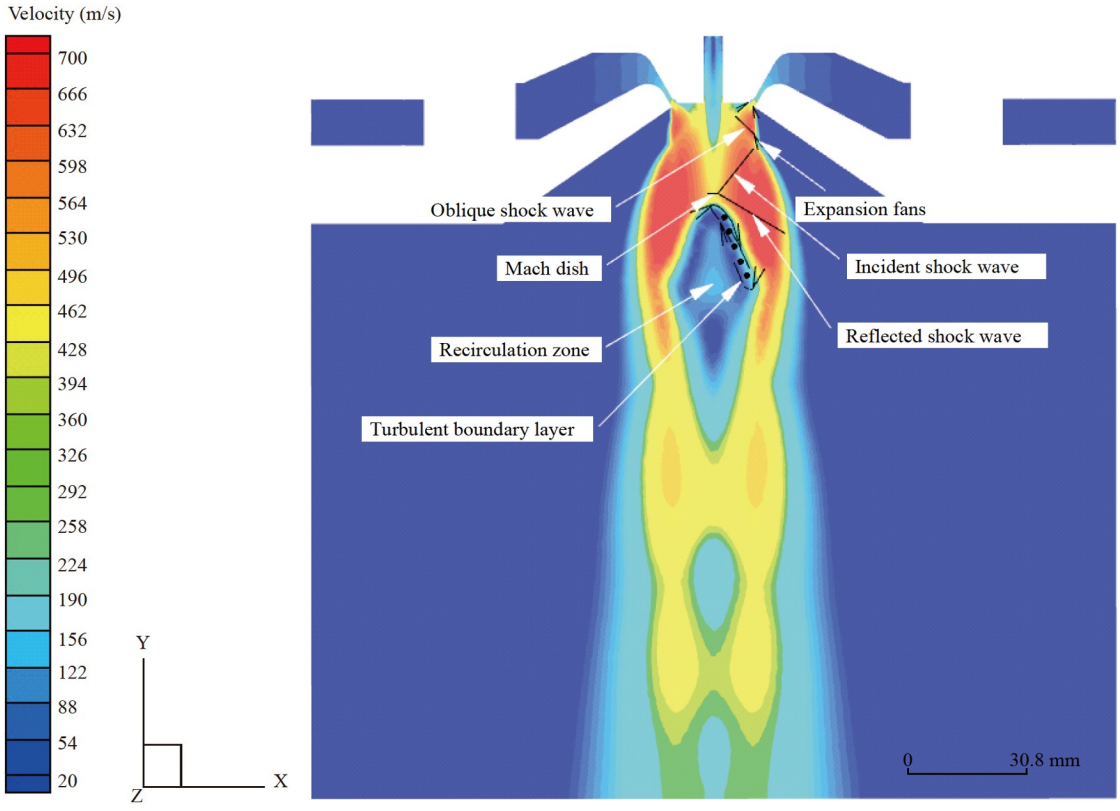

Figure 5 Calculated results for the atomized droplets in the gas flow field before incidence.

velocity surface in the annular slit, which locates at the minimum throat section area. Atomized gas flow in the atomizer may expand continuously in the annular slit until reaching the gas outlet of the annular slit at an accelerated speed after passing through this sound velocity surface. When the atomized gas flow is ejected from the gas outlet of the annular slit, the atomized gas flow ejected from the gas outlet of the annular slit may continue to expand and accelerate to make the static pressure of atomized jet reaches a balance with the static pressure phase in the atomizing chamber. The atomized gas flow after expansion and acceleration might advance toward the downstream at a high speed, thus forming an atomizing jet area with clear boundaries. The inner side of the atomizing jet is adjacent to the atomizing gas near the front end of the MDT, while the outside contacts with surrounding supplying gases. The atomizing gas flow which expands outward slightly forms a series of high-intensity oblique shock waves after rebounding by the external environmental gases which are almost static. Since atomizing gas near the front end of the MDT has a relatively high speed along the same direction with environmental gases under the effect of atomizing jet, a series of weak oblique shock waves are formed at the inner side of the atomizing jet. When atomizing gas flow passes through these oblique shock waves, it will be decelerated, accompanied with volume shrinkage. It intersects with the tail of the first oblique shock wave at the outer side of atomizing gas flow. Moreover, the first Mach disk and a reflection shock wave appear in the intersection area. The RZ at downstream of the first Mach disk in the gas flow field is explicit and there is the turbulent boundary layer at edges of the RZ.

The distribution law of the tangential speed of the atomizing gas at the front end of the MDT along the radial direction is shown in Fig. 6. Clearly, with the increase of radial distance to the central axis, the tangential speed of atomizing gas at the front end of the MDT increases quickly to the maximum and then decreases gradually. This reflects the fact that the atomized droplets flying are affected by the centrifugal force and they always point to the wall of the atomizing chamber along the radial direction. The maximum

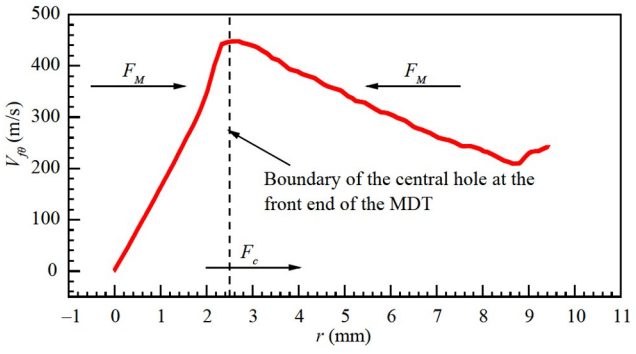

Figure 6 Tangential speed $V_{f\theta}$ distribution of the atomizing gas at the front end of the MDT.

tangential speed of atomizing gas (449 m/s) occurs near the point where its distance to the central axis is equal to the radius of the central hole. Combining this with the definition of the Magnus effect, it is found that in the region where the tangential speed of atomizing gas increases along the radial direction, the Magnus force, which acts on the discrete-phase atomized droplets from the continuous-phase atomizing gas, points to the wall of the atomizing chamber along the radial direction. In the region where the tangential speed of atomizing gas decreases along the radial direction, the Magnus force which is acted on the discrete-phase atomized droplets by continuous-phase atomizing gas points to the central axis along the radial direction.

The distribution law of static pressure intensity of atomizing gas at the front end of the MDT along the radial direction is shown in Fig. 7. Obviously, with the increase of radial distance to the central axis, the static pressure intensity of atomizing gas at the front end of the MDT in the atomizing chamber increases gradually, accompanied with the gradual growth of radial pressure gradient. This indicates that the radial pressure gradient force always points to the central axis along the radial direction and that it is positively correlated with the radial distance to the central axis.

The distribution law of the static temperature of atomizing gas at the front end of the MDT along the radial direction is shown in Fig. 8. Clearly, with the increase of radial distance to the central axis, the static temperature of atomizing gas at the front end of the MDT in the atomizing chamber decreases quickly to the minimum. Meanwhile, the radial temperature gradient drops sharply and then increases gradually, accompanied with the gradual reduction of radial temperature gradient (this is mainly caused by the change of the tangential speed of atomizing gas at the front end of the MDT with the increase of radial distance to the central axis). According to the definition of the thermophoretic force, it found that in the region where the static temperature of atomizing gas decreases along the radial direction, the

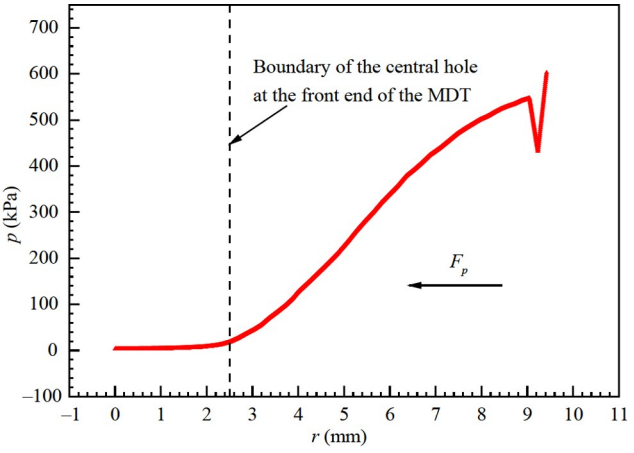

Figure 7 Static pressure intensity p distribution of the atomizing gas at the front end of the MDT.

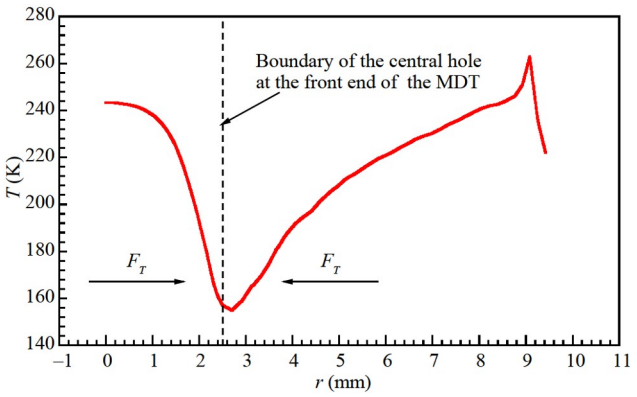

Figure 8 Static temperature T distribution of the atomizing gas at the front end of the MDT.

thermophoretic force which is applied by the continuous-phase atomizing gas onto the discrete-phase atomized droplets points to the wall of the atomizing chamber along the radial direction. Moreover, it increases with the increase of radial distance to the central axis of the gas flow field. In the region where the static temperature of atomizing gas increases along the radial direction, the thermophoretic force which is applied by the continuous-phase atomizing gas onto the discrete-phase atomized droplets points toward the central axis along the radial direction. It is negatively correlated with the radial distance to the central axis.

The distribution law of axial speed of atomizing gas on the central axis in the atomizing chamber along the negative direction of the y-axis is shown in Fig. 9. Clearly, with the increase of distance to the front end of the MDT along the negative direction of y-axis, the axial speed of atomizing gas on the central axis in the atomizing chamber increases

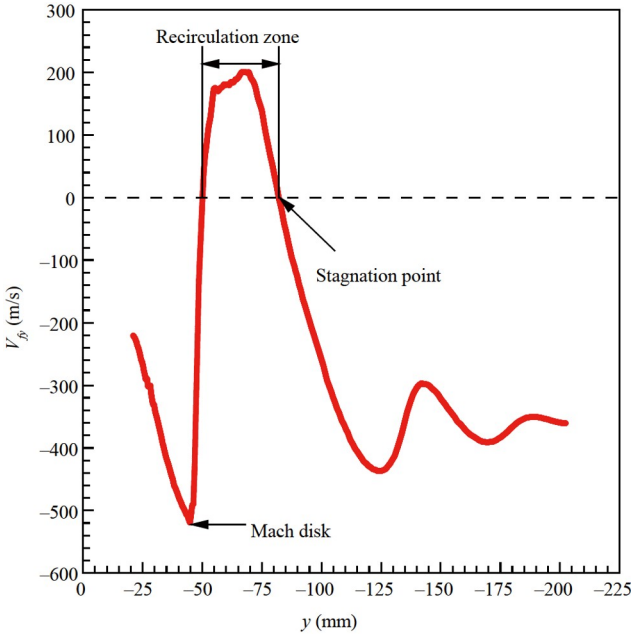

Figure 9 Axial speed V_{fy} distribution of the atomizing gas on the central axis.

gradually to the peak (the position of the Mach disk) and then drops sharply to 0 m/s (the front end of the RZ). After passing the RZ, the axial speed of atomizing gas increases gradually again from 0 m/s (SP) and finally makes consistent fluctuations near the peak. This indicates that the influence of atomizing gas on the axial movement of atomized droplets in the swirling flow field is very complicated. The maximum axial speed of atomizing gas occurs near the point where is 23.8 mm away from the front end of the MDT and it values 519.4 m/s.

The atomized droplets enter into the gas flow field from the source position as shown in Fig. 10. Since the initial speed of atomized droplets is far lower than the flow rate of atomizing gas, it will be affected by surrounding atomizing gas. The separation-related gas speed distribution in the spherical surface boundary layer in the transverse free incoming flow is shown in Fig. 11. Clearly, $u_\infty(x)$ is used to express the flow rate of free incoming gas in relative to the sphere in the built spherical coordinate system. Since $u_\infty(0) = 0$ m/s at the front SP, gas near the windward surface of the sphere undergoes accelerated movement under the effect of a forward-pressure gradient (when $\mathrm{d}p/\mathrm{d}x < 0$, $\mathrm{d}u/\mathrm{d}x > 0$). In this process, the gas velocity-type shape in the boundary layer becomes increasingly "full", from point *A* to point *B* in Fig. 11. When $\mathrm{d}p/\mathrm{d}x = 0$, gas speed in the flow field reaches the maximum. Subsequently, gas makes decelerated movement under the effect of the reversed pressure gradient (when $\mathrm{d}p/\mathrm{d}x > 0$, $\mathrm{d}u/\mathrm{d}x < 0$). In this process, the gas velocity-type shape in the boundary layer becomes "thinner and thinner", as shown from point *B* to point *D* in Fig. 11. With the reduction of gas speed near the windward side of the sphere, gas velocity gradient ($\partial u/\partial y\big|_{y=0}$) on the spherical surface finally decreases to 0, as shown in point *D* in Fig. 11. The position where the gas velocity gradient on the spherical surface changes to zero is called as the separation point.

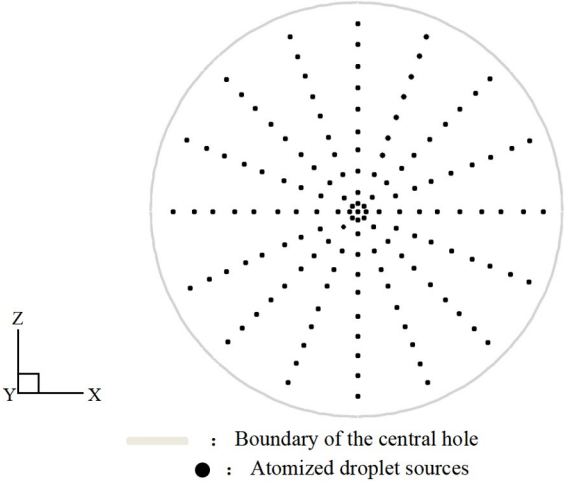

Figure 10 Distribution of atomized droplet sources on the central hole section at the front end of the MDT.

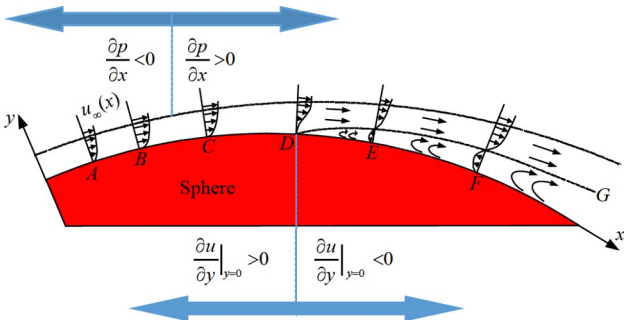

Figure 11 Separation-related gas speed distribution in the spherical surface boundary layer in the transverse free incoming flow.

Since the momentum of gases near the wall at the separation point is insufficient to overcome the influence of the reversed pressure gradient, recirculation gas opposing the direction of the free incoming flow occurs near the downstream spherical surface. This will push the gas in the boundary layer coming from the upstream continuously away from the spherical surface and squeeze it toward the external potential flow area, ultimately causing the separation of the boundary layers, as shown from point *D* to point *E* in Fig. 11. After the boundary layer is separated, gases which are separated from the spherical surface are injected into the external potential flow and a separation surface is formed on the interface between the external potential flow zone and the separation zone, which is shown by the dotted *DG* in Fig. 11. Since gas separation on a spherical surface will affect the stresses of the sphere significantly, the flowing separation on the spherical surface should be analyzed thoroughly.

Since the Reynolds number (*Re*) determines the occurrence of the boundary layer transition, it has a strong influence on the position of separation points of the boundary layer. Since the characteristic length of the sphere is equal to the diameter, Re_D of a sphere is defined as follows:

$$Re_D = \frac{\rho_f u'_{fp} D_s}{\mu} = \frac{u'_{fp} D_s}{\nu}, \tag{15}$$

where u'_{fp} is the gas speed relative to the sphere and D_s is the diameter of the sphere.

One study [27] demonstrated that if $0 < Re_D \leq 2\times10^5$, the gas flow inside the boundary layer of the spherical surface takes the form of a laminar flow and the separation of the boundary layer occurs at a point where is about 80° from the front SP. If $Re_D \geq 2\times10^5$, a boundary layer transition may occur, thus delaying the boundary layer separation from the spherical surface to a point that is about 140° from the front SP.

The above process influences the resistance on the sphere (F_d) significantly. F_d has two components. One is the tangential stress (frictional resistance) applied by the boundary layer onto the spherical surface. The other is the pressure difference (shape or pressure difference resistance) along the flowing direction which is caused by the formation of the

wake flow zone. F_d can be expressed as

$$F_d = C_d A_f \frac{\rho_f u_{fp}^2}{2}, \tag{16}$$

where A_f is the windward area of the sphere (the projection area perpendicular to the free incoming flow velocity).

When $0 < Re_D \leq 2$, influences of boundary layer separation from the spherical surface can be ignored. The flowing state of gases inside the boundary layer is mainly controlled by the frictional resistance of the wall surface. However, this state mainly occurs at the end of the flying of atomized droplets during LA. It is not discussed in this study. When $Re_D \geq 2\times10^5$, C_d drops sharply.

In the droplet motion, the Stokes number (St) is a very important parameter. St is defined as the ratio of the particle momentum response time (τ_p) over a flow system time (τ_c), defined as

$$St = \frac{\tau_p}{\tau_c} = \frac{\rho_p d_p^2 V_f}{18\mu R}, \tag{17}$$

where R indicates the radius of the spray (= 0.105 m). Two types of situations can be observed for particles (bubbles/droplets) suspended in fluid [28].

Since atomized droplets that enter into the gas flow field from the source position have a small initial flying speed and it can be ignored in relative to the speed of atomizing gas, the speed of atomizing gas can be viewed as the relative speed between atomized droplets and atomizing gas. In this study, N_2 was used as the atomizing gas. Under room temperature, $\mu = 18.4\times10^{-6}$ Pa s or kg/(m s) and $\rho_f = 1.25$ kg/m^3. The atomized droplets are melting-state pure Al metals (the detailed physical attributes are introduced in Ref. [26]). The critical gas speeds corresponding to atomized droplets with different diameters when $Re_D = 2$, $Re_D = 2\times10^5$, and $St_D = 1$ are shown in Table 1. Results showed that the relative flying speeds of all atomized droplets are all between the upper and lower limits the critical gas speed, and the critical gas speed is negatively related with the diameter of atomized droplets when $St_D = 1$. The variation curve of resultant velocity (V_f) of atomizing gas on the central axis of the flow field along the negative direction of y-axis is shown in Fig. 12. Clearly, V_f has a range of about 300-500 m/s in the flying interval of the atomized droplets, but it is relatively smaller near the front end of the MDT, in the region between the Mach disk and the front end of the RZ, in the RZ, and at the SP. According to Eq. (15), in the gas flow field gained under the same initial conditions, Re is positively correlated with the diameter of atomized droplets. Combining this with the relationship between the Re of the sphere and its resistance coefficient (see Fig. 13), it can be concluded that the resistance coefficient of the atomizing gas against atomized droplets is negatively correlated with the Re of the atomized droplets. In other words, larger atomized droplets have smaller resistance coefficients, while smaller atomized droplets have larger resistance coefficients. This reveals that smaller atomized droplets are easier to go with flows ($St_D \ll 1$). This is also proven by the numerical simulation results presented in the following.

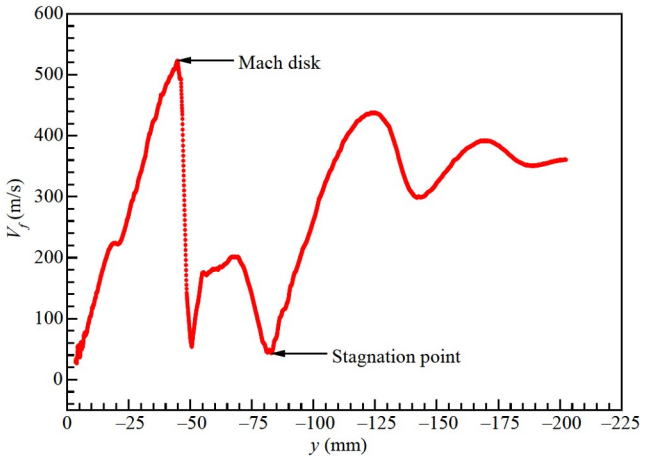

Figure 12 Resultant velocity V_f distribution of the atomizing gas on the central axis.

4. Two-phase flow analysis of atomized droplets in the gas flow field

4.1 Effects of the diameter of atomized droplets

The flight trajectories of atomized droplets with different diameters (3-30 μm) incident on the swirling flow field from the source position at a speed of 50 m/s are shown in Fig. 14 ($0.0311 < St_D < 3.106$). Clearly, at the droplets source, the

Table 1 Critical gas speeds of atomized droplets with different diameters

Droplet diameter (μm)	$Re_D = 2$ Critical gas speed (m/s)	$Re_D = 2\times10^5$ Critical gas speed (m/s)	$St_D = 1$ Critical gas speed (m/s)
3	9.813	9.813×10^5	1610
5	5.888	5.888×10^5	579.6
7	4.206	4.206×10^5	295.714
10	2.944	2.944×10^5	144.9
20	1.472	1.472×10^5	36.225
30	0.981	0.981×10^5	16.1
40	0.736	0.736×10^5	9.056
50	0.589	0.589×10^5	5.796
60	0.491	0.491×10^5	4.025

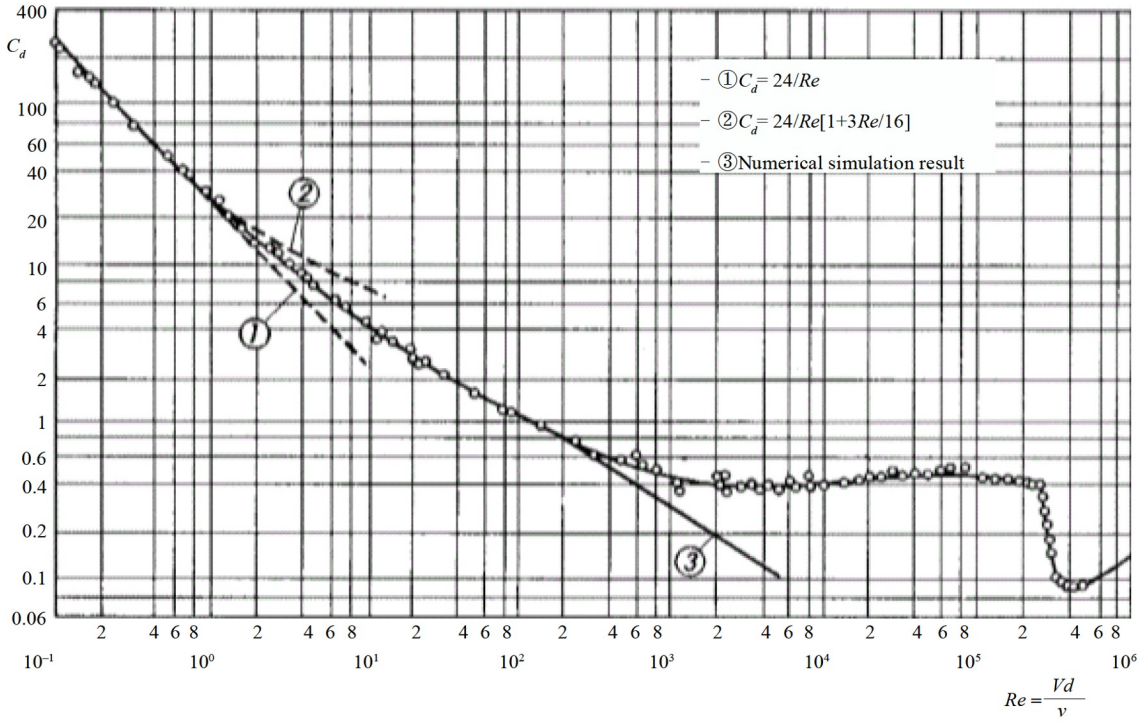

Figure 13 Variation curve of the C_d of a sphere with Re [27].

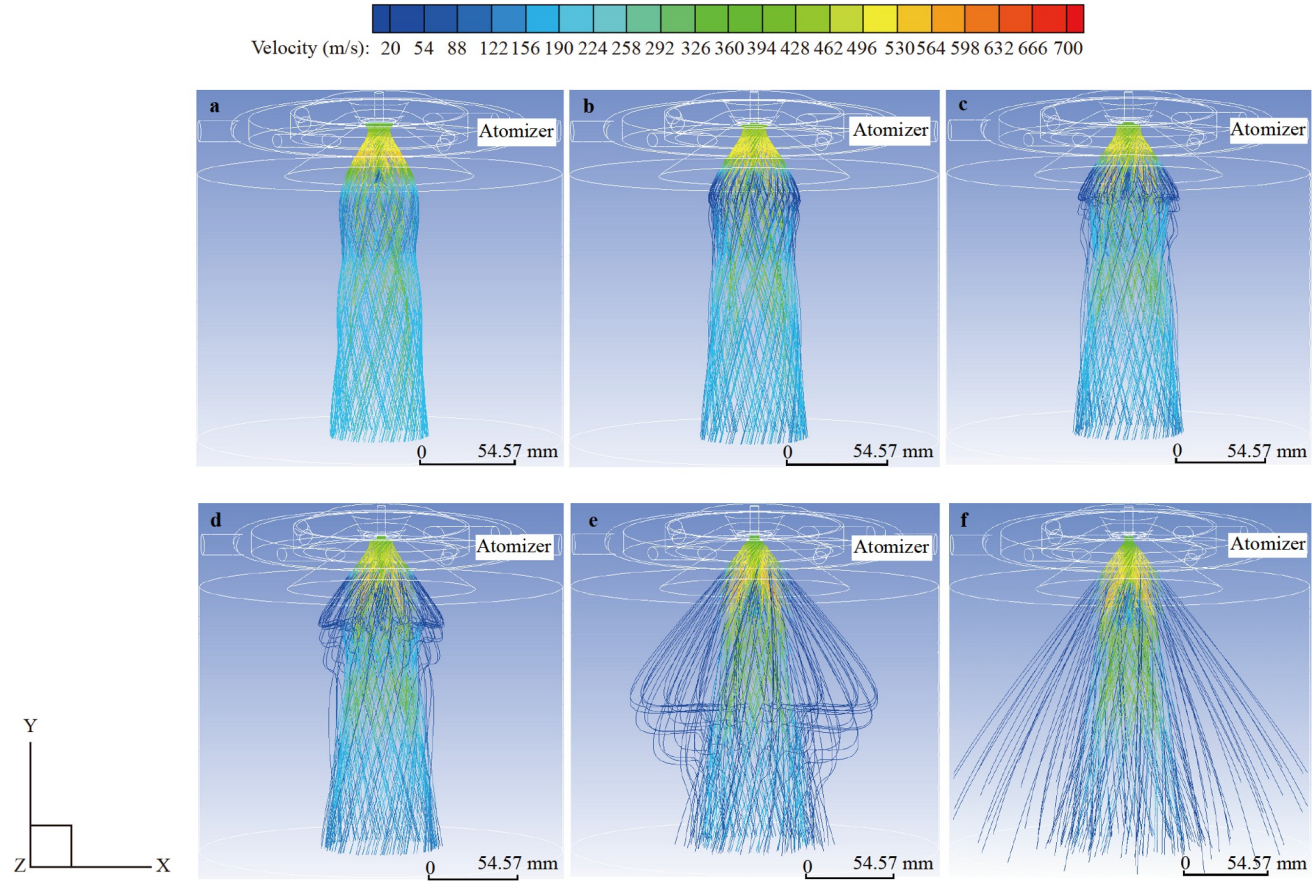

Figure 14 Flight trajectories of atomized droplets (diameter < 30 μm), one of the curves represents the flight trajectory of a droplet: **a** d_p = 3 μm, **b** d_p = 5 μm, **c** d_p = 7 μm, **d** d_p = 10 μm, **e** d_p = 20 μm, and **f** d_p = 30 μm.

radial paving scope of atomized droplets which are far away from the central axis and enter into the swirling flow field from the source position expands at the front end of the MDT. This is mainly caused by different stresses on atomized droplets that enter into the swirling flow field from different sources at the front end of the MDT. It can be seen from Figs. 6, 8, and 13 that given the higher radial Magnus force and thermophoretic force on atomized droplets that are far away from the central axis and enter into the swirling flow field from the source position at the front end of the MDT as well as tangential drag force of atomizing gas, the tangential speed of atomized droplets increases, thus increasing the radial centrifugal force and finally making them distant away along the radial direction.

Additionally, Fig. 14 shows that the radial pavement scope of these atomized droplets at the front end of the MDT is negatively correlated with their diameter. At the outlet boundary in the computational domain, the radial pavement scope of larger atomized droplets is larger, which is mainly attributed to different stresses on atomized droplets with different diameters in the flying region. It can be seen from Figs. 6, 8, and 13 that larger atomized droplets that enter into the swirling flow field from the same source bear the smaller radial Magnus force, thermophoretic force, and drag force coefficient of atomizing gas at the front end of the MDT, thus getting the smaller tangential speed and thereby resulting in the smaller centrifugal force. It also can be seen from Fig. 7 that larger atomized droplets bear the stronger radial pressure gradient force, finally resulting in their smaller radial movement distance at the front end of the MDT. However, larger atomized droplets have stronger kinetic energies, making their flying trajectories in the swirling flow field difficult to be interfered. The flying trajectories of smaller atomized droplets are easier to be restricted by the swirling flow field since they bear the stronger resistance coefficient of atomizing gas and have the smaller kinetic energy. Finally, the radial pavement scope of larger atomized droplets at the outlet boundary in the computational domain is larger.

The flying trajectories of atomized droplets with different diameters (3-30 μm) incident in the swirling flow field from the source position at a speed of 50 m/s near the RZ are shown in Fig. 15. Obviously, atomized droplets entering into the swirling flow field from the source position nearer to the central axis are affected more by the movement of atomizing gas near the RZ. This can be explained as follows. Since the movement of these atomized droplets along the negative direction of the *y*-axis is completely hindered by the drag

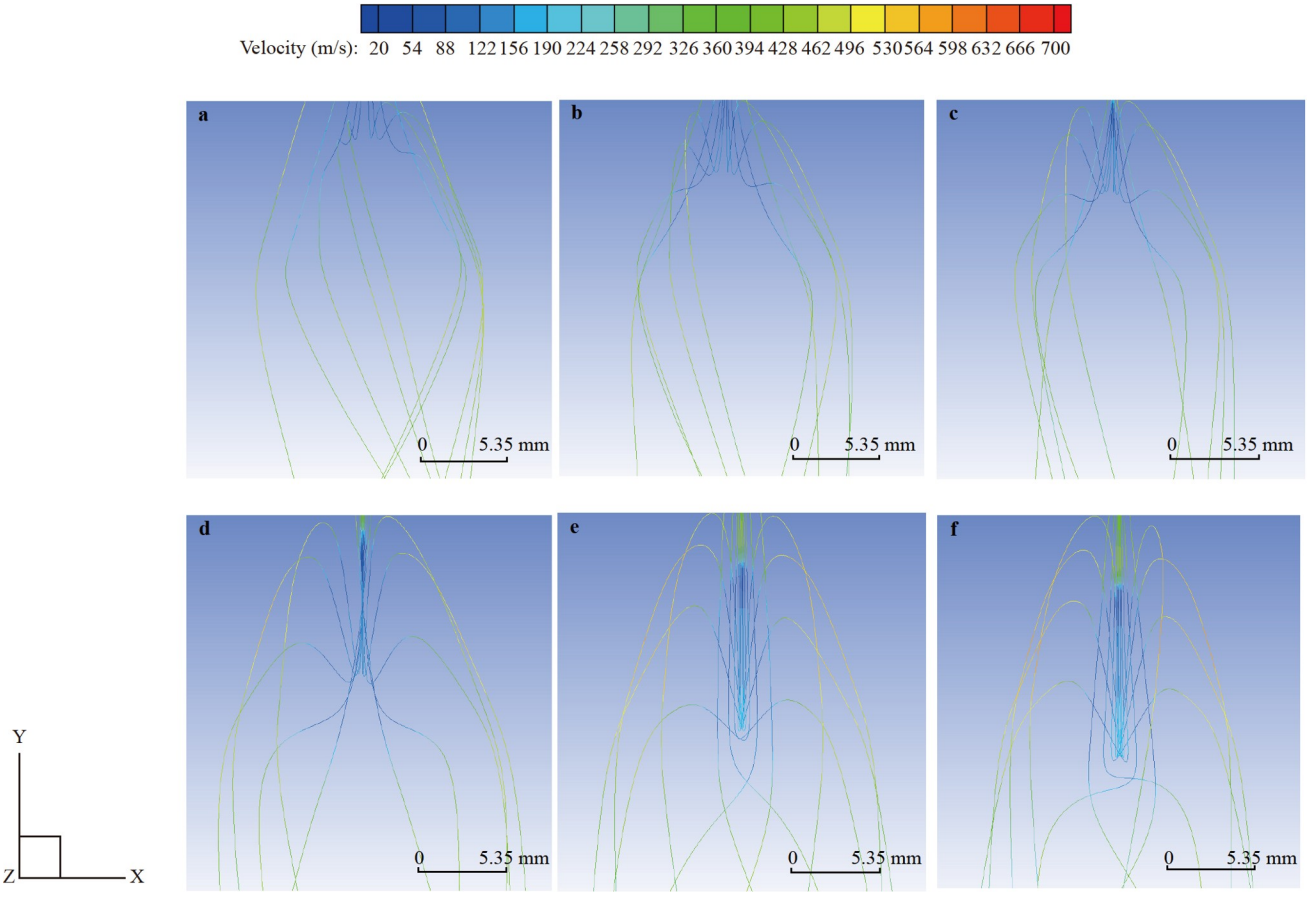

Figure 15 Flight trajectories of atomized droplets (diameter < 30 μm) near the RZ, one of the curves represents the flight trajectory of a droplet: **a** d_p = 3 μm, **b** d_p = 5 μm, **c** d_p = 7 μm, **d** d_p = 10 μm, **e** d_p = 20 μm, and **f** d_p = 30 μm.

force of atomizing gas which is near the central line of the RZ and moves along the positive direction of the *y*-axis, these atomized droplets move along the positive direction of the *y*-axis. Differently, atomized droplets that enter into the swirling flow field from the source position far away from the central axis are pushed to the outer edges of the RZ by the drag force of atomizing gases which are moving along the radial and tangential directions near and in the RZ. Moreover, the atomized droplets which are closer to the central axis are pushed further away in the beginning stage of the radial movement. This can be explained according to the first theorem of Helmholtz. Since atomizing gases in the RZ have the greater angular velocity of rotation at positions closer to the central axis, atomized droplets near the RZ and closer to the central axis of the gas flow field get the higher tangential speed component and thereby bear the stronger centrifugal force. As a result, atomized droplets closer to the central axis have the longer radial movement distance in the initial stage. During the practical LA under the above situations, although the metal melt which flows into the swirling flow field from the central hole will not continue to move along the negative direction of the *y*-axis after they come close to the RZ, the metal melt will spread radially under the collaborative effect of gravity, drag force of atomizing gas, centrifugal force, and radial pressure gradient force. This is the cause of the above sheet breakup model.

Moreover, Fig. 15 shows that flying trajectories of larger atomized droplets are closer to the central axis near and in the RZ. This is mainly because larger atomized droplets bear the smaller centrifugal force due to the greater kinetic energy as well as the smaller Magnus force, thermophoretic force, and resistance coefficient of the atomizing gas. Consequently, the flight trajectories of larger atomized droplets in the swirling flow field have stronger anti-inference capabilities and are easier to move closer to the central axis. Eventually, the flight trajectories of larger atomized droplets near and in the RZ approach to the central axial. When the diameter of atomized droplets is large enough to overcome the drag force of the atomizing gas in the RZ which is moving along the positive direction of the *y*-axis, tangential and radial directions by their own kinetic energy, atomized droplets will run through the RZ completely along the negative direction of the *y*-axis.

The flying trajectories of atomized droplets within the scope of 40-50 μm incident in the swirling flow field from the source position at a speed of 50 m/s are shown in Fig. 16 ($5.521 < St_D < 8.627$). It can be seen from Fig. 16 that along the negative direction of the *y*-axis, the radial diversion range of larger atomized droplets decreases gradually. This is mainly because larger atomized droplets have greater kinetic energies and undertake the smaller resistance coefficient from the atomizing gas, thus suffering smaller centrifugal force. As a result, their flying trajectories in the swirling flow field come closer and closer to the central axis. Eventually, the radial diversion tendency of the larger atomized droplets becomes smaller.

The flying trajectories of atomized droplets within the scope of 40-50 μm incident in the swirling flow field from the source position at a speed of 50 m/s near the RZ are shown in Fig. 17. Clearly, near the central axis of the RZ, the flying trajectories of larger atomized droplets are closer to the central axis of the RZ, and they can better overcome influences of drag force from the atomizing gas in the RZ which is moving along the positive direction of the *y*-axis. This can be explained as follows. With the increase of the diameter of atomized droplets, the kinetic energy increases continuously, while the Magnus force, thermophoretic force, and resistance coefficient of atomizing gas decrease continuously. Hence, these atomized droplets are subject to a smaller centrifugal force and average drag force from the atomizing gas. They have the stronger ability to maintain the original flying trajectory. Consequently, the flying trajec-

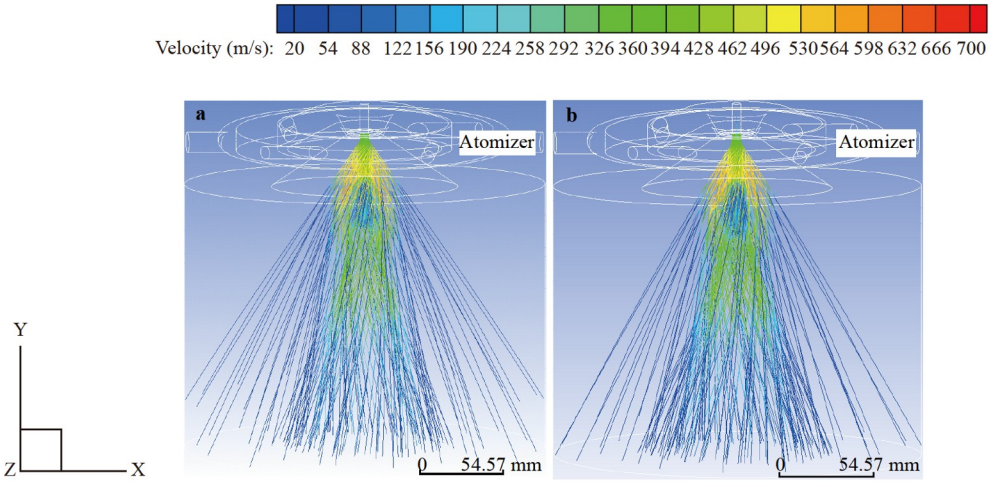

Figure 16 Flight trajectories of atomized droplets within the range of 40-50 μm, one of the curves represents the flight trajectory of a droplet: **a** $d_p = 40$ μm and **b** $d_p = 50$ μm.

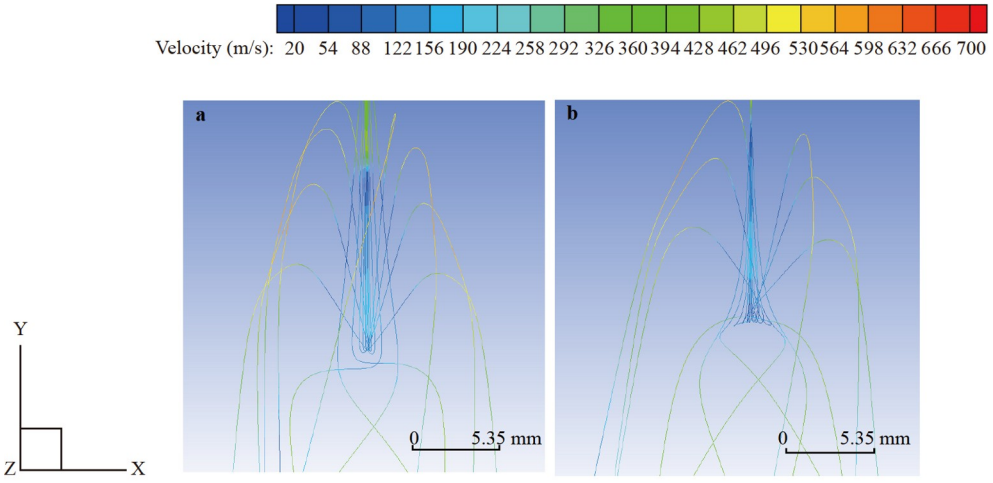

Figure 17 Flight trajectories of atomized droplets within the range of 40-50 μm near the RZ, one of the curves represents the flight trajectory of a droplet: **a** d_p = 40 μm and **b** d_p = 50 μm.

tories of larger atomized droplets near the RZ are concentrated at the central axis of the RZ. Moreover, due to the continuous volume growth of atomized droplets near the central axis of the RZ, the growth rate of kinetic energies of atomized droplets is higher than that of drag force from the atomizing gas in the RZ which is moving along the positive direction of the *y*-axis when flying trajectories of atomized droplets are approaching to the central axis of the RZ. Hence, larger atomized droplets can resist the drag force of atomizing gas in the RZ which is moving along the positive direction of the *y*-axis better.

When the diameter of atomized droplets increases to 60 μm (St_D = 12.422), atomized droplets in the swirling flow field which are near the RZ can completely overcome the drag force of the atomizing gas in the RZ which are moving toward the positive direction of *y*-axis, tangentially and radially. Therefore, these atomized droplets run through the RZ along the negative direction of the *y*-axis. Under this circumstance, influences of the RZ in the swirling flow field on the flying trajectories of atomized droplets can be ignored (see Fig. 19a). Differently, the flying trajectories of atomized droplets that are flying in the swirling flow field out of the RZ are less probably to diverge radially due to the greater kinetic energy and smaller resistance coefficient of atomizing gas (see Fig. 18a). During practical LA, in the above situation, a metal melt that flows into the swirling flow field from the central hole will continue to undergo fluctuating breakup in the additional rotational flow along the negative direction of the *y*-axis under the collaborative effects of gravity and the atomizing gas flow. The entire LA process may not be influenced by the RZ in the swirling flow field. This is the cause of the above-described fluctuating breakup model.

When the diameter of the atomized droplets continues to increase to 65 μm (St_D = 14.579), the flying trajectories of atomized droplets in the swirling flow field are basically consistent with those of atomized droplets when the diameter is 60 μm except for the decreased range of radial

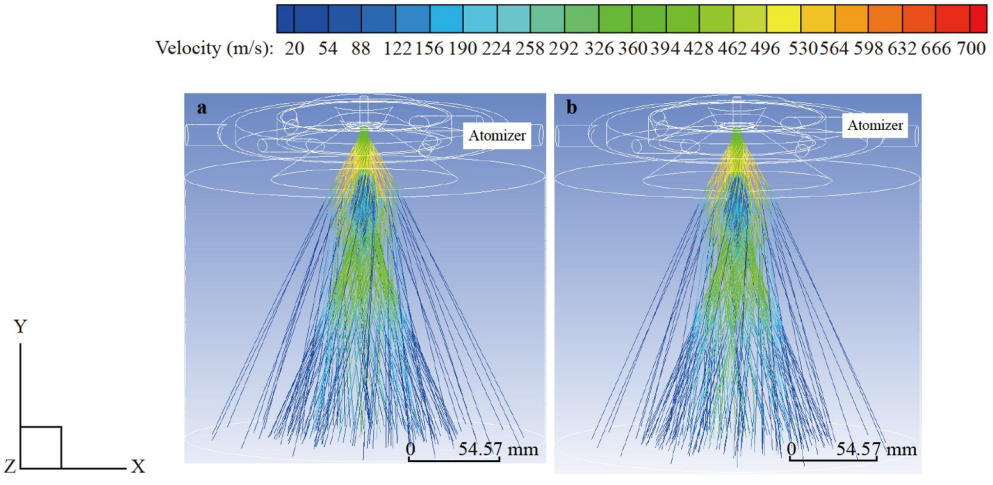

Figure 18 Flight trajectories of large atomized droplets (diameter > 60 μm), one of the curves represents the flight trajectory of a droplet: **a** d_p = 60 μm and **b** d_p = 65 μm.

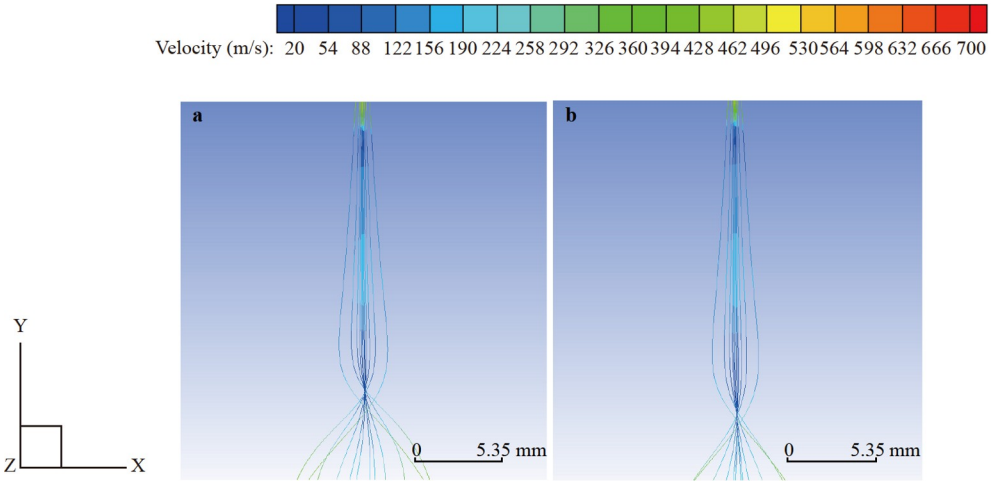

Figure 19 Flight trajectories of large atomized droplets (diameter > 60 μm) near the RZ, one of the curves represents the flight trajectory of a droplet: **a** d_p = 60 μm and **b** d_p = 65 μm.

divergence (see Figs. 18b and 19b). To sum up, large atomized droplets (diameter > 60 μm) which enter from the same source position into the swirling flow field at an incident speed of 50 m/s have basically consistent flying trajectories under the geometric structure of the atomizer and atomizing technological parameters in this study.

4.2 Effects of the incident speed of the atomized droplets

The flying trajectories of atomized droplets (diameter = 45 μm) which enter into the swirling flow field from the source position at different incident speeds (40-75 m/s) are shown in Fig. 20 ($5.59 < St_D < 10.481$). Clearly, along the negative direction of the *y*-axis in the swirling flow field, the flying trajectories of atomized droplets with greater incident speeds have the smaller radial spreading scope. Reasons are introduced as follows. Atomized droplets with a greater incident speed have greater kinetic energy, which makes their initial flying trajectories difficult to be interfered. Subsequently, the atomized droplets can easily move along the negative direction of the *y*-axis. Finally, flying trajectories of atomized droplets with greater incident speeds approach to the central axial of the gas flow field.

The flying trajectories of atomized droplets (diameter = 45 μm) which enter into the swirling flow field from the source position at different incident speeds (40-75 m/s) near the RZ are shown in Fig. 21. Clearly, when the incident speed is 40 m/s, atomized droplets in the swirling flow field which approaches to the RZ cannot run through the RZ along the negative direction of the *y*-axis due to the insufficient kinetic energy to resist the drag force of atomizing gas in the RZ which moves along the positive direction of the *y*-axis. Influenced by the drag forces of atomizing gas near and in the RZ which makes tangential and radial movement, these atomized droplets move along the edges of the RZ radially.

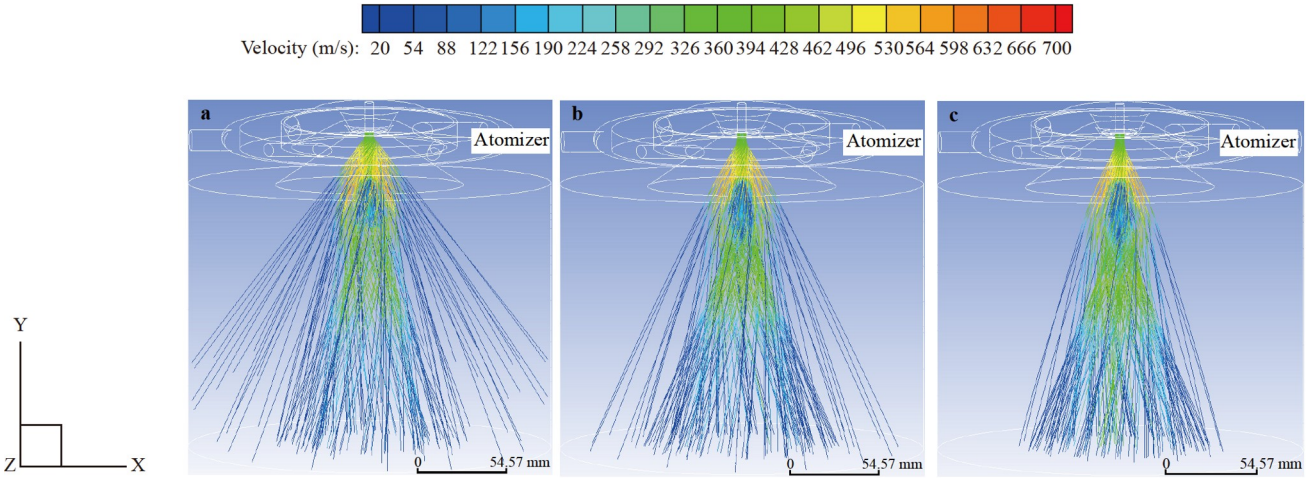

Figure 20 Flight trajectories of atomized droplets with different incident speeds, one of the curves represents the flight trajectory of a droplet: **a** V_p = 40 m/s, **b** V_p = 60 m/s, and **c** V_p = 75 m/s

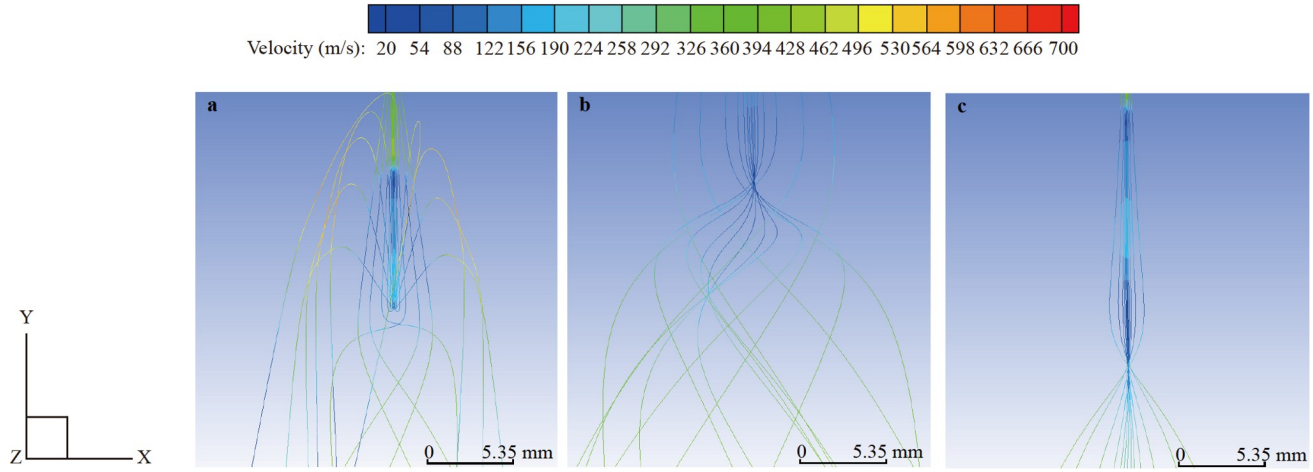

Figure 21 Flight trajectories of atomized droplets with different incident speeds near the RZ, one of the curves represents the flight trajectory of a droplet: **a** V_p = 40 m/s, **b** V_p = 60 m/s, and **c** V_p = 75 m/s.

When the incident speed increases to 60 m/s, atomized droplets in the swirling flow field which approach to the RZ can run through the RZ along the negative direction of the *y*-axis completely since the kinetic energy increases to be able to resist the drag force of the atomizing gas in the RZ which moves along the positive direction of the *y*-axis. Nevertheless, they still cannot eliminate influences of drag forces of atomizing gas which makes tangential and radial movement near the RZ completely (this is mainly caused by the decreased kinetic energy of atomized droplets to resist the drag force of the atomizing gas in the RZ). Hence, these atomized droplets continue to move along the radial direction near the RZ and the atomized droplets closer to the central axis of the gas flow field show the longer radial movement distance in the initial stage. In a word, the Helmholtz first theorem is still true near the RZ under this flowing condition.

When the incident speed increases to 75 m/s, atomized droplets in the swirling flow field that approach the RZ have enough kinetic energy to overcome the drag force of atomizing gas in the RZ which is moving along the positive direction of the *y*-axis. Therefore, they can run through the RZ completely along the negative direction of the *y*-axis. With the increase of incident speed of atomized droplets, the flying speeds of atomized droplets near the RZ increase under the effect of the atomizing gas flow, which shortens the time to run through the RZ along the negative direction of the *y*-axis. As a result, the influencing time of atomizing gas under radial and tangential movement on the atomized droplets near and in the RZ is shortened accordingly. Eventually, the radial movement distance of the atomized droplets which fly near the RZ along the negative direction of *y*-axis decreases when they pass through the recirculation region. In a word, the flying trajectories of atomized droplets under initial parameters are affected by the RZ slightly, which almost can be ignored.

5. Conclusions

In this study, the flight trajectories of metal Al droplets in the swirling gas flow field of a close-coupled vortical atomizer under different initial parameter values were analyzed based on the analysis of the single-phase flow field characteristics of the gas. Some major conclusions could be drawn:

(1) At the droplets source, the radial paving scope of atomized droplets which are far away from the central axis and enter into the swirling flow field from the source position expands at the front end of the MDT. The radial pavement scope of these atomized droplets at the front end of the MDT is negatively correlated with their diameter. At the outlet boundary in the computational domain, when d_p < 30 μm, the radial pavement scope of larger atomized droplets is larger, and when d_p > 30 μm, the radial diversion range of larger atomized droplets decreases gradually.

(2) The flight trajectories of atomized droplets with smaller diameters or incident speeds (St_D (1) are more easily affected by the atomizing gas in the swirling flow field. When the incident speed is 50 m/s, atomized droplets with a diameter larger than 60 μm (St_D > 12.422) can pass through the RZ along the negative direction of the *y*-axis. Moreover, their flight trajectories are influenced only slightly by the RZ, which can almost be ignored. For atomized droplets with a fixed diameter, the ability to maintain the flight trajectory is positively correlated with the incident speed (the St_D number increases gradually). In other words, atomized droplets with a higher incident speed pass more easily through the RZ along the negative direction of the *y*-axis. This reveals that the RZ in the gas flow field of the vortical atomizer and the kinetic energy of the atomized droplets can significantly influence their flight trajectories in the swirling flow field.

(3) During practical LA, a vortical atomizer has two metal melt breakup models—the fluctuating breakup and the sheet breakup. This is determined by the collaborative effect of

the gravity of the metal melt, which flows into the atomizing chamber from the central hole, the drag force of the atomizing gas, the centrifugal force, and the radial pressure gradient force. These results can provide a reference for the classification of the atomization models of a vortical atomizer in the real LA process. In addition, whether the fluctuating breakup model is the "micro-fountain" breakup model needs further verification and research.

Author contributions *Min Zhang designed the research and wrote the first draft of the manuscript. Zhaoming Zhang and Qiusheng Liu helped organize the manuscript. Min Zhang and Qiusheng Liu revised and edited the final version.*

Acknowledgements *This work was supported by the National Natural Science Foundation of China (Grant Nos. 11532015 and U1738119) and the Priority Academic Program Development of Jiangsu Higher Education Institutions (PAPD).*

1 H. W. Ouyang, X. Chen, W. T. Yu, et al., Progress and prospect on the gas atomization, Powder Metall. Technol. **25**, 53 (2007).
2 A. G. Dowson, Atomization dominates powder production, Metal Powder Report **54**, 15 (1999).
3 J. Ting, M. W. Peretti, and W. B. Eisen, The effect of wake-closure phenomenon on gas atomization performance, Mater. Sci. Eng.-A **326**, 110 (2002).
4 J. Ting, and I. E. Anderson, A computational fluid dynamics (CFD) investigation of the wake closure phenomenon, Mater. Sci. Eng.-A **379**, 264 (2004).
5 H. W. Ouyang, B. Y. Huang, X. Chen, and W. T. Tao, Melt metal sheet breaking mechanism of close-coupled gas atomization, T. Nonferr. Metal. Soc. **15**, 985 (2005).
6 W. J. Zhao, Study on the Gas Flow Field in Spray Deposition and the Breakup Mechanism, Dissertation for Doctoral Degree (Harbin Institute of Technology, Harbin, 2012).
7 S. H. Wang, Y. C. Fang, and D.G. Zhao, Numerical simulation of liquid metal primary atomization in gaseous swirling flow field (in Chinese), China Powder Sci. Technol. **22**, 7 (2016).
8 K. Hanthanan Arachchilage, M. Haghshenas, S. Park, L. Zhou, Y. Sohn, B. McWilliams, K. Cho, and R. Kumar, Numerical simulation of high-pressure gas atomization of two-phase flow: Effect of gas pressure on droplet size distribution, Adv. Powder Tech. **30**, 2726 (2019).
9 S. Luo, H. Wang, Z. Gao, Y. Wu, and H. Wang, Interaction between high-velocity gas and liquid in gas atomization revealed by a new coupled simulation model, Mater. Des. **212**, 110264 (2021).
10 M. Zhang, Z. M. Zhang, Y. Q. Zhang, and Y. J. Lu, CFD-based numerical simulation of gas flow field characteristics in close-coupled vortical loop slit gas atomization, Atomiz. Spr. **31**, 17 (2021).
11 M. Zhang, Z. M. Zhang, Y. Q. Zhang, Y. J. Lu, and L. Lu, Effects of gas flow field on clogging phenomenon in close-coupled vortical loop slit gas atomization, Trans. Nanjing Univ. Aero. Astro. **38**, 1003 (2021).
12 G. Strotos, I. Malgarinos, N. Nikolopoulos, and M. Gavaises, Predicting droplet deformation and breakup for moderate weber numbers, Int. J. Multiphase Flow **85**, 96 (2016).
13 D. I. Meiron, G. R. Baker, and S. A. Orszag, Analytic structure of vortex sheet dynamics, Part 1. Kelvin-Helmholtz instability, J. Fluid Mech. **114**, 283 (1982).
14 C. J. Gurney, The Stability and Control of Curved Liquid Jet Break-Up, Dissertation for Doctoral Degree (University of Birmingham, Birmingham, 2010).
15 S. P. Mates, and G. S. Settles, A study of liquid metal atomization using close-coupled nozzles, part 1: Gas dynamic behavior, Atomiz. Spr. **15**, 19 (2005).
16 S. P. Mates, and G. S. Settles, A study of liquid metal atomization using close-coupled nozzles, part 2: Atomization behavior, Atomiz. Spr. **15**, 41 (2005).
17 E. A. Ibrahim, and E. T. Akpan, Three-dimensional instability of viscous liquid sheets, Atomiz. Spr. **6**, 649 (1996).
18 D. Beckers, N. Ellendt, U. Fritsching, and V. Uhlenwinkel, Impact of process flow conditions on particle morphology in metal powder production via gas atomization, Adv. Powder Tech. **31**, 300 (2020).
19 Y. Chen, H. Xiong, H. Cheng, C. Yu, and J. Xie, Effect of particle motion on the hydraulic collection of coarse spherical particles, Acta Mech. Sin. **36**, 72 (2020).
20 Z. G. Cai, J. H. Pan, and M. J. Ni, The evolution and instability of wake structure around an impulsively stopped sphere with a streamwise magnetic field for $600 \leq Re \leq 1400$, Acta Mech. Sin. **38**, 322070 (2022).
21 J. Listewnik, in Some factors influence the performance of de-oiling hydrocyclones for marine applications: Proceedings of 2nd International Conference on Hydrocyclones, Bath, 1984.
22 L. J. Guo, Two-Phase and Multi-Phase Flow Dynamics (Xi'an Jiaotong University Press, Xi'an, 2002).
23 L. S. Fan, and C. Zhu, Principles of Gas-Solid Flows (Cambridge University Press, Cambridge, 1998).
24 P. A. Moreno-Casas, and F. A. Bombardelli, Computation of the basset force: Recent advances and environmental flow applications, Environ. Fluid Mech. **16**, 193 (2015).
25 M. Pilch, C. A. Erdman, and A. B. Reynolds, Acceleration Induced Fragmentation of Liquid Drops (The Commission, Brussels, 1981).
26 M. Zhang, and Z. Zhang, Numerical simulation study on cooling of metal droplet in atomizing gas, Mater. Today Commun. **25**, 101423 (2020).
27 H. Schlichting, and K. Gersten, Boundary-Layer Theory, 9th ed. (Springer-Verlag, Berlin, Heidelberg, 2017).
28 C. T. Crowe, Multiphase Flow Handbook (CRC Press, Florida, 2006).

紧耦合旋涡环缝式雾化器的初级液体雾化机理研究

章敏, 张召明, 刘秋生

摘要 为了初步探究紧耦合旋涡环缝式雾化器在真实条件下的液体雾化过程, 本文在对旋涡环缝式雾化器气体单相流场特性分析的基础上对金属熔体破碎后形成的并不再继续破碎的雾化液滴在旋流场中的飞行轨迹进行基于离散相模型的数值模拟. 研究结果表明: 在雾化室内导液管前端中心孔液滴源位置处, 自距气流场中心轴线距离越远的液滴源进入旋流场中的雾化液滴在导液管前端径向铺展范围越大. 自雾化室内导液管前端中心孔液滴源进入旋流场中的雾化液滴其直径越大则在导液管前端沿径向铺展的范围越小. 气流场中的回流区域和雾化液滴自身动能对雾化液滴在旋流场中的飞行轨迹有很大的影响, 并且旋涡环缝式雾化器对金属熔体存在两种破碎模式, 即波动破碎模式和膜状破碎模式. 模拟结果可为旋涡环缝式雾化器在真实液体雾化过程中雾化模式的分类提供参考.